

CRYO-EM AS A STOCHASTIC INVERSE PROBLEM*

DIEGO SANCHEZ ESPINOSA[†], ERIK HENNING THIEDE[‡], AND YUNAN YANG[§]

Abstract. Cryo-electron microscopy (Cryo-EM) enables high-resolution imaging of biomolecules, but structural heterogeneity remains a major challenge in 3D reconstruction. Traditional methods assume a discrete set of conformations, limiting their ability to recover continuous structural variability. In this work, we formulate cryo-EM reconstruction as a stochastic inverse problem (SIP) over probability measures, where the observed images are modeled as the push-forward of an unknown distribution over molecular structures via a random forward operator. We pose the reconstruction problem as the minimization of a variational discrepancy between observed and simulated image distributions, using statistical distances such as the KL divergence and the Maximum Mean Discrepancy. The resulting optimization is performed over the space of probability measures via a Wasserstein gradient flow, which we numerically solve using particles to represent and evolve conformational ensembles. We validate our approach using synthetic examples, including a realistic protein model, which demonstrates its ability to recover continuous distributions over structural states. We analyze the connection between our formulation and Maximum A Posteriori (MAP) approaches, which can be interpreted as instances of the discretize-then-optimize (DTO) framework. We further provide a consistency analysis, establishing conditions under which DTO methods, such as MAP estimation, converge to the solution of the underlying infinite-dimensional continuous problem. Beyond cryo-EM, the framework provides a general methodology for solving SIPs involving random forward operators.

Key words. cryo-EM, stochastic inverse problem, Wasserstein gradient flow, particle method, push-forward map

MSC codes. 65M32, 49Q22, 65M75, 65K10

1. Introduction. Understanding the molecular structure of biomolecules is fundamental for elucidating their function, dynamics, and interactions. Cryo-electron microscopy (Cryo-EM) has emerged as a transformative technology for characterizing the structures of biomolecules [19, 26, 11, 45]. In cryo-EM experiments, thousands to millions of individual particles, rapidly frozen in vitreous ice, are imaged by a transmission electron microscope. Traditional data analysis pipelines then attempt to reconstruct the underlying three-dimensional (3D) structure from the ensemble of noisy two-dimensional (2D) projections [43, 22]. Due to advances in detector technology, electron optics, and sample preparation, experimentalists can then recover biomolecular structures to sub-nanometer, or even atomic, resolutions [18, 30, 35, 12].

However, one of the major complications in cryo-EM is structural heterogeneity—the fact that biomolecules, such as proteins, often adopt multiple shapes or dynamic conformations even under the same experimental conditions. This results in a single dataset containing a mixture of different structural states, which must be disentangled to understand the molecule’s functional mechanisms. Moreover, this heterogeneity is not just an experimental nuisance: it has considerable biological importance. Many proteins adopt different conformations: a specific arrangement of atoms in 3D space. Changes between conformations regulate many cellular processes, from enzyme catalysis to signal transduction [49, 14, 23]. Characterizing these changes enables the development of targeted therapeutics [27], informs mutagenesis experiments, and deepens our understanding of disease mechanisms at the atomic scale [16]. Addressing this heterogeneity is crucial for resolving biologically meaningful states and understanding functional mechanisms. Traditional reconstruction pipelines, such as those implemented in RELION [40, 39] and cryoSPARC [36, 38], typically rely on discrete classification schemes, which assume that all biomolecules adopt one of a finite number of conformations. While widely used and effective for well-separated states, these methods are often believed to be insufficient for capturing smooth or continuous

*Submitted to the editors.

Funding: This work is partially supported by the National Science Foundation through grant DMS-2409855 and by the Office of Naval Research through grant N00014-24-1-2088.

[†]Center for Applied Mathematics, Cornell University, Ithaca, NY (ds973@cornell.edu).

[‡]Department of Chemistry, Cornell University, Ithaca, NY (eht45@cornell.edu).

[§]Department of Mathematics, Cornell University, Ithaca, NY (yunan.yang@cornell.edu)

structural variability.

This belief has motivated the development of approaches aimed at heterogeneity as a continuum of structures, typically by attempting to recover an underlying low-dimensional manifold of states.

Prior work has attempted to recover these low-dimensional manifolds using a combination of techniques, such as diffusion maps [20, 34], linear dimensionality reduction [36], or neural networks [52, 28]. We refer interested readers to [47] for a detailed discussion.

Recent work has taken a different approach: rather than attempting to collect a set of representative structures or a representative low-dimensional motion, one attempts to approximate the probability distribution over all possible conformations.

This statistical perspective enables not only the identification of the most probable states but also the characterization of the underlying energy landscape. For instance, Tang et al. (2023) [46] propose an ensemble reweighting approach that adjusts the weights of a prior ensemble of atomic structures, typically obtained from molecular dynamics or structure prediction, according to their agreement with the observed images, yielding a posterior distribution over conformations. In contrast, RECOVAR [21], introduced by Gilles and Singer (2025), bypasses the need for atomic models by estimating the mean and covariance of the 3D conformational distribution directly from the projection images. A low-dimensional embedding is then constructed via Principal Component Analysis (PCA), and a density is inferred using kernel density estimation, corrected for observational noise. In both approaches, the resulting density is linked to the free energy via the Boltzmann probability density and the assumption that freezing is instantaneous, enabling a physically meaningful interpretation of conformational preferences.

Our approach builds on this direction by introducing a non-parametric framework for cryo-EM reconstruction formulated as a stochastic inverse problem (SIP) in the space of probability measures [6, 8, 9, 10, 33, 32]. Specifically, we assume that the observed images form an empirical probability distribution which arises as the push-forward of an unknown latent distribution over molecular structures under a random forward map. Rather than inferring a finite ensemble of conformations, we cast this as a variational problem: we seek the structural distribution that minimizes a statistical discrepancy between the predicted image distribution and the observed empirical image distribution. This formulation captures the uncertainty inherent in image generation and reframes cryo-EM reconstruction as a principled optimization over the space of probability distributions. This SIP shares similarities with Bayesian inverse problems [44]. However, whereas in Bayesian inverse problems we seek to model the distribution of possible parameter values, here we seek to recover a probability distribution that is itself a scientific object of interest, independent of any measurement noise or uncertainty.

To define this variational problem, we introduce a generalized loss functional that quantifies the difference between probability distributions over the image space. The loss function may take the form of established statistical distances such as the Maximum Mean Discrepancy (MMD) and the Kullback–Leibler (KL) divergence. This loss is computed between the observed empirical distribution of cryo-EM images and the simulated image distribution produced by applying the generative image formation process to the candidate structural distribution. This formulation allows us to go beyond pointwise or likelihood-based reconstruction for the structures and instead reason about distributions directly. We then optimize this loss function over the distributions of structures by applying a Wasserstein gradient flow.

This approach allows us to compute gradient-like updates to the distribution over biomolecular structures using the geometry of optimal transport, providing a natural descent direction even in infinite-dimensional spaces. The resulting gradient flow is discretized using a particle-based approximation, allowing us to represent and evolve a set of structural samples that collectively approximate the optimal distribution. This scheme retains flexibility in representing conformations while benefiting from the stability and regularity of the Wasserstein gradient flow.

Our work also provides new insights into existing research that attempts to recover structures through maximum likelihood or maximum a posteriori (MAP) estimation. We show that, in the appropriate limits, these methods can be viewed as attempts to recover the probability density over structures as well. These pipelines employ a discretize-then-optimize (DTO) strategy, approximating the conformational distribution through a finite mixture of discrete volumes and subsequently optimizing the discretized model. By contrast, our method follows an optimize-then-discretize (OTD) paradigm: we first solve a variational problem over the space of probability measures, and only discretize the result when needed for downstream tasks. We further establish theoretical connections between these two paradigms by identifying conditions under which DTO-based reconstructions converge to the OTD formulation. The OTD paradigm allows us to model structural heterogeneity in a more flexible and principled way, without prematurely restricting the solution space to a finite-dimensional subset. Furthermore, it enables the interpretation and numerical analysis of the reconstructed structural distribution with respect to the image data size and discretization parameters.

The structure of this work is as follows. In Section 2, we review the mathematical background of stochastic inverse problems, as well as the gradient flow framework for solving the resulting variational problem on an infinite-dimensional probability space tailored to the random push-forward map characteristic of the cryo-EM problem. In Section 3, we discuss the OTD and DTO approaches to formulating the inverse problem, including a consistency analysis that connects MAP-based DTO methods (e.g., RELION) with our proposed OTD framework. Section 4 presents three numerical examples: a one-dimensional test system, an example depicting heterogeneity in nanoclusters, and an example depicting realistic protein motion, demonstrating the effectiveness of our approach. We conclude with discussions in Section 5.

2. Cryo-EM as a Stochastic Inverse Problem. In a cryo-EM experiment, a solution containing many copies of a protein is snap-frozen into a thin layer of amorphous water. This layer is then placed under an electron microscope, allowing practitioners to collect many images, each displaying a protein viewed at a random rotation. For instance, a simplified model for the cryo-EM imaging pipeline is given by

$$(2.1) \quad y = T(\theta, \omega) = H^{\omega_r} \theta + \omega_n,$$

where H^{ω_r} is a linear operator on the space of 3D structures that incorporates a random rigid motion in $SO(3)$, an orthographic projection onto the z -axis, and convolution with the microscope’s point-spread function. The random variable ω has two independent components, $\omega = (\omega_n, \omega_r)$. The noise term ω_n is additive Gaussian noise, $\omega_n \sim \mathcal{N}(0, \sigma^2 I)$, while ω_r encodes the random imaging geometry and is distributed according to a measure ρ_{ω_r} .

Traditional approaches to cryo-EM assume that every image depicts a protein in the same structure: effectively, that all images are generated from the same θ . Algorithms then attempt to recover this single structure from experimental data. However, real proteins adopt a multitude of structures.

While historically variability in the structure was seen as an experimental nuisance, increasingly more work has observed that this variability is of scientific interest in its own right. To understand this variability, we follow [46] and take the probability distribution over structures as our central object of study. Given the empirical distribution of observed images ρ_y , our objective is to infer the distribution of underlying molecular structures ρ_θ via the *random* parameter-to-observable map (2.1). This inference task is challenging: depth information is lost in the projection, the viewing directions are latent, and the signal-to-noise ratio is often extremely low, all contributing to the difficulty of recovering ρ_θ , the probability distribution for the protein structures. These challenges motivate us to consider a new approach for cryo-EM.

Below, we present our primary theoretical contributions of this work: we formalize recovering the distribution ρ_θ as a stochastic inverse problem, relax it to a variational problem, and show how this variational problem can be solved using gradient flows.

2.1. From Deterministic to Stochastic Inverse Problems. In a deterministic inverse problem, a forward operator $T : \Theta \rightarrow R \subseteq Y$, maps an element θ in the parameter space Θ to the data space Y , where $R = T(\Theta)$ denotes the range of T . The observed data $y^\delta \in Y$ may contain noise such that y^δ does not lie in the range R .

In stochastic inverse problems (SIPs) [6, 33], the unknown parameter is lifted from a single point in the set Θ to a probability distribution over Θ that lies in the set $\mathcal{P}(\Theta)$, which consists of all probability distributions defined over Θ . Data also become distributions over Y that live in $\mathcal{P}(Y)$.

Often, the operator F that maps the parameter distribution to the data distribution is a push-forward operator $F = T_\#$ where the map $T : \Theta \rightarrow Y$ is a deterministic forward map. In these setups, the observed data distribution is the push-forward measure of the parameter distribution in $\mathcal{P}(\Theta)$. We give the definition of the push-forward measure below.

DEFINITION 2.1. (Push-Forward Measure). *Let (X, \mathcal{A}) and (Y, \mathcal{B}) be measurable spaces, and let $f : X \rightarrow Y$ be a measurable function. The push-forward measure $f_\# \mu$ of μ under f is a measure on Y defined by*

$$f_\# \mu(B) = \mu(f^{-1}(B)),$$

for all $B \in \mathcal{B}$, the σ -algebra of set Y .

We address two common scenarios where the push-forward measure can be easily understood.

- If μ is absolutely continuous with respect to the Lebesgue measure, it is associated with a probability density function $\rho(x)$ such that $d\mu(x) = \rho(x)dx$. If f is a differentiable bijection, then the push-forward measure $f_\# \mu$ is also associated with a probability density function $\tilde{\rho}(x)$ where the relationship between $\rho(x)$ and $\tilde{\rho}(x)$ can be understood through the change-of-variable formula $\rho(x) = \tilde{\rho}(f(x))\det(\nabla f)$.
- Consider $\mu = \sum_{i=1}^N w_i \delta_{x_i}$, a weighted sum of Dirac deltas, for $N \in \mathbb{N}$, $\sum_{i=1}^N w_i = 1$ and $w_i \geq 0$. Then the push-forward measure has the explicit form

$$f_\# \mu = \sum_{i=1}^N w_i \delta_{f(x_i)}.$$

That is, the push-forward map does not change the weight of the samples, but geometrically moves the support of the sample from $x_i \in X$ to $f(x_i) \in Y$.

2.2. General Stochastic Inverse Problem. While most SIPs in the literature are formulated using a deterministic push-forward operator, in cryo-EM and other relevant applications [50], the forward operator incorporates a random push-forward map T_ω , where ω is a random variable with distribution μ_ω .

For each realization $\hat{\omega}$ drawn from μ_ω , the induced map $T_{\hat{\omega}} : \Theta \rightarrow Y$, pushes the parameter probability distribution ρ_θ to the data probability distribution over the Y domain. One can also view $T_{\hat{\omega}}$ as a map parameterized by $\hat{\omega}$, which motivates us to use the following notations T_ω , T_θ and T hereafter:

$$y = T_\omega(\theta) \iff y = T(\omega, \theta) \iff y = T_\theta(\omega).$$

Let ρ_y^δ be our observed data distribution with δ highlighting the presence of noise δ . The forward operator that maps a given parameter distribution ρ_θ to the corresponding predicted data distribution ρ_y can be expressed as

$$\begin{aligned} \rho_y &= F(\rho_\theta) \\ (2.2) \quad &= T_\#(\mu_\omega \otimes \rho_\theta) = \iint \delta_{y=T(\hat{\omega}, \hat{\theta})} d\mu_\omega(\hat{\omega}) d\rho_\theta(\hat{\theta}) \end{aligned}$$

$$(2.3) \quad = \int T_{\hat{\omega} \#} \rho_\theta d\mu_\omega(\hat{\omega})$$

$$(2.4) \quad = \int T_{\hat{\theta} \#} \mu_\omega d\rho_\theta(\hat{\theta}).$$

We write our forward operator in these three equivalent ways with different interpretations:

- In (2.2), the data distribution ρ_y is a push-forward measure from the joint distribution $\mu_\omega \otimes \rho_\theta$ by the map T . This perspective reduces to those discussed in [6, 33]. In particular, $\pi(y, \hat{\omega}, \hat{\theta})$ is the joint distribution of all three variables where

$$(2.5) \quad d\pi(y, \hat{\omega}, \hat{\theta}) = \delta_{y=T(\hat{\omega}, \hat{\theta})} d\mu_\omega(\hat{\omega}) d\rho_\theta(\hat{\theta})$$

while ρ_y is regarded as the marginal distribution of π after integrating over the $\hat{\omega}$ and $\hat{\theta}$ variables.

- In (2.3), the data distribution is a weighted ensemble of all realizations of the push-forward measure $T_{\hat{\omega}} \# \rho_\theta$ based on the law μ_ω . More precisely, $T_{\hat{\omega}} \# \rho_\theta$ is the marginal distribution of π after integrating over the $\hat{\theta}$ variable.
- In (2.4), the data distribution is a weighted ensemble of all realizations of the push-forward measure $T_{\hat{\theta}} \# \rho_\omega$ based on the law ρ_θ . Since ρ_θ showed up as the integration measure, (2.4) is quite favorable when representing ρ_θ as an empirical measure. Similarly, $T_{\hat{\theta}} \# \rho_\omega$ is the marginal distribution of the joint distribution π in (2.5) after integrating over the $\hat{\omega}$ variable.

The goal of the SIP is to recover ρ_θ , given a noisy observed distribution ρ_y^δ , the law μ_ω and the forward operator (2.2), (2.3) or (2.4).

If we assume that T is invertible with an executable map T^{-1} and the data distribution ρ_y^δ is in the range of the map $T_\#$, we can solve the inverse problem directly through

$$\mu_\omega^* \otimes \rho_\theta^* = (T^{-1})_\# \rho_y^\delta.$$

However, in almost all interesting inverse problems, T is not invertible. For example, in cryo-EM, T is a projection operator whose output dimension is strictly lower than the input dimension; see Equation (2.1). On the other hand, the fact that T^{-1} does not exist does not necessarily imply that F is not invertible or that the SIP is ill-posed. This extra layer of difficulty and complication makes us turn to a variational framework to solve the inverse problem computationally.

2.3. The Variational Framework. Due to the presence of noise and the nonlinearity of the forward map F , one can relax this infinite-dimensional SIP (2.3) to a variational problem, for which we can apply a wide range of optimization strategies to practically reconstruct the unknown parameter distribution. The variational problem takes the form

$$(2.6) \quad \inf_{\rho_\theta \in \Omega \subset \mathcal{P}(\Theta)} E(\rho_\theta), \quad E(\rho_\theta) = D(F(\rho_\theta), \rho_y^\delta),$$

where the search domain Ω is a subset of $\mathcal{P}(\Theta)$, with the latter representing all probability measures over the domain Θ , and D quantifies the discrepancy between ρ_y^δ and $F(\rho_\theta)$. Under suitable conditions about the coercivity of the set Ω and the lower semicontinuity of the objective function $E(\rho_\theta)$ [31], the minimizer of the variational problem exists and the ‘‘inf’’ in (2.6) can be replaced by the ‘‘min’’. We thus assume such conditions hold and all variational problems admit a minimizer hereafter.

The space of probability distributions is not a linear space. The constraint of non-negativity and the conservation of mass, as well as its central role in fields such as statistics and probability, have given rise to a wide range of geometries. Below, we give a few examples of metrics and divergences that can be used to for D .

DEFINITION 2.2. (*p*-Wasserstein metric). *Let (\mathcal{X}, d) be a metric space, and let μ and ν be two probability measures on \mathcal{X} with finite p -th order moments. The p -Wasserstein distance (also known as the W_p metric) between μ and ν is defined by*

$$W_p(\mu, \nu) = \left(\inf_{\gamma \in \Gamma(\mu, \nu)} \int_{\mathcal{X} \times \mathcal{X}} d(x, y)^p d\gamma(x, y) \right)^{1/p},$$

where $\Gamma(\mu, \nu)$ denotes the set of all couplings of μ and ν . A coupling γ is a probability measure on $\mathcal{X} \times \mathcal{X}$ such that for all measurable subsets $A, B \subseteq \mathcal{X}$, $\gamma(A \times \mathcal{X}) = \mu(A)$ and $\gamma(\mathcal{X} \times B) = \nu(B)$.

The W_p metric measures the minimal ‘‘cost’’ of transporting mass from one distribution to another, where the cost is given by the distance to the p power, $d(x, y)^p$, between x and y .

DEFINITION 2.3. (*f*-divergence). *Let (Ω, \mathcal{F}) be a measurable space, and let μ and ν be two probability measures on this space such that μ is absolutely continuous with respect to ν (denoted $\mu \ll \nu$). Let $f : (0, \infty) \rightarrow \mathbb{R}$ be a convex function with $f(1) = 0$. The *f*-divergence between μ and ν is defined by*

$$D_f(\mu \parallel \nu) = \int_{\Omega} f\left(\frac{d\mu}{d\nu}(x)\right) d\nu(x),$$

where $\frac{d\mu}{d\nu}$ is the Radon–Nikodym derivative of μ with respect to ν .

Different choices of the convex function f yield various well-known divergences. In particular, the Kullback–Leibler (KL) divergence corresponds to $f(t) = t \ln t - t + 1$:

$$(2.7) \quad D_{\text{KL}}(\mu \parallel \nu) = \int_{\Omega} \ln\left(\frac{d\mu}{d\nu}(x)\right) d\mu(x).$$

In addition, we will also consider the so-called Maximum Mean Discrepancy (MMD).

DEFINITION 2.4. (Maximum Mean Discrepancy). *Let $k : \mathcal{X} \times \mathcal{X} \rightarrow \mathbb{R}$ be a continuous, symmetric, positive-definite kernel function. Let μ and ν be two probability distributions defined on \mathcal{X} . The Maximum Mean Discrepancy (MMD) between μ and ν is defined by*

$$(2.8) \quad \text{MMD}(\mu, \nu) = \sqrt{\mathbb{E}_{x, x' \sim \mu}[k(x, x')] + \mathbb{E}_{y, y' \sim \nu}[k(y, y')] - 2\mathbb{E}_{x \sim \mu, y \sim \nu}[k(x, y)]}.$$

It can be shown that $\text{MMD}(\mu, \nu) \geq 0$, and the choice of kernel k affects the sensitivity of MMD to differences between two distributions. Given samples $\{x_i\}_{i=1}^m$ from μ and $\{y_j\}_{j=1}^n$ from ν , an unbiased empirical estimator of the squared MMD is

$$\widehat{\text{MMD}}^2 = \frac{1}{m(m-1)} \sum_{i \neq i'} k(x_i, x_{i'}) + \frac{1}{n(n-1)} \sum_{j \neq j'} k(y_j, y_{j'}) - \frac{2}{mn} \sum_{i, j} k(x_i, y_j).$$

The above formula makes the MMD loss both practical and effective for quantifying discrepancies between empirical measures, without requiring density estimation, a very appealing feature in high-dimensional settings.

We will use the so-called *energy distance* [41] in our numerical section.

$$(2.9) \quad D_E(\mu, \nu) = \sqrt{2\mathbb{E}_{x \sim \mu, y \sim \nu}[\|x - y\|] - \mathbb{E}_{x, \tilde{x} \sim \mu}[\|x - \tilde{x}\|] - \mathbb{E}_{y, \tilde{y} \sim \nu}[\|y - \tilde{y}\|]}.$$

It is a special MMD with the kernel $k(x, y) = -\|x - y\| + \|x\| + \|y\|$.

2.4. Gradient Flow Equations. We need a computationally feasible way to solve the infinite-dimensional optimization problem (2.6). One of the most common approaches is gradient descent or, in the limit of infinitesimal step sizes, a gradient flow. Gradient is not derivative, and the performance of gradient descent depends highly on the metric space of the parameter under consideration.

Since our optimization problem is formulated over the space of probability distributions, a good choice of metric is important. For instance, taking the L^2 gradient flow would yield the following partial differential equation (PDE)

$$\partial_t \rho_{\theta}(\theta, t) = -\frac{\delta E(\rho_{\theta})}{\delta \rho_{\theta}}(\theta, t),$$

whose solution does not preserve positivity and mass conservation, which are essential structures of probability distributions.

In this work, we focus on the quadratic Wasserstein distance (W_2) as the geometry to define gradients; see Definition 2.2 with $p = 2$. The choice is not unique, but we focus on W_2 because it naturally leads to an intuitive and effective particle method, as detailed below.

We use $\frac{\delta E(\rho_\theta)}{\delta \rho_\theta}$ to denote the first-order variation of the objective function E with respect to the parameter distribution ρ_θ . The Wasserstein gradient flow equation then takes the form

$$\begin{aligned}
 \partial_t \rho_\theta(\theta, t) &= \nabla_\theta \cdot \left(\rho_\theta(\theta, t) \nabla_\theta \frac{\delta E(\rho_\theta)}{\delta \rho_\theta} \right) \\
 &= \nabla_\theta \cdot \left(\rho_\theta(\theta, t) \nabla_\theta \left(\int \frac{\delta D}{\delta \rho_y}(T_{\hat{\omega}}(\theta)) d\mu_\omega(\hat{\omega}) \right) \right) \\
 (2.10) \quad &= \nabla_\theta \cdot \left(\rho_\theta(\theta, t) \left(\int \nabla T_{\hat{\omega}}^\top \nabla_y \frac{\delta D}{\delta \rho_y}(T_{\hat{\omega}}(\theta)) d\mu_\omega(\hat{\omega}) \right) \right),
 \end{aligned}$$

where $\frac{\delta D}{\delta \rho_y}$ is the first-order variation of $D(\rho_y, \rho_y^\delta)$ with respect to ρ_y , which can be seen as a function of y , and $\nabla T_{\hat{\omega}}^\top$ is the transpose of the Jacobian of the forward map $T_{\hat{\omega}}$ for a fixed realization of $\hat{\omega}$.

One key observation is that Equation (2.10) is the continuity equation with the velocity

$$- \int \nabla T_{\hat{\omega}}^\top \nabla_y \frac{\delta D}{\delta \rho_y}(T_{\hat{\omega}}(\theta)) d\mu_\omega(\hat{\omega}).$$

Thanks to the equivalence between Lagrangian and Eulerian perspectives on fluid modeling:

$$\frac{dx}{dt} = v(x, t) \quad (\text{Lagrangian ODE}) \quad \text{and} \quad \partial_t \rho + \nabla \cdot (v\rho) = 0 \quad (\text{Eulerian PDE}),$$

Equation (2.10) naturally gives rise to a deterministic ensemble particle method for numerical simulation:

$$(2.11) \quad \frac{d}{dt} \theta_i(t) = - \int \nabla T_{\hat{\omega}}^\top \nabla_y \frac{\delta D}{\delta \rho_y}(T_{\hat{\omega}}(\theta_i(t))) d\mu_\omega(\hat{\omega}), \quad 1 \leq i \leq N,$$

where $\rho_\theta(\theta, t) \approx \frac{1}{N} \sum_{i=1}^N \delta_{\theta_i(t)}(\theta) =: \hat{\rho}_\theta$. Equation (2.11) is classified as an ensemble particle method because $\frac{\delta D}{\delta \rho_y}$ depends on $F(\hat{\rho}_\theta)$, which incorporates contributions from all particles $\{\theta_i\}_{i=1}^N$.

Here is a concrete numerical algorithm to solve the gradient flow equation (2.10) using the particle method (2.11) based on a simple forward Euler time-stepping scheme:

- Step 1 Draw N samples $\{\theta_i(0)\}_{i=1}^N$ from the initial parameter distribution $\rho_\theta(\theta, 0)$. Set time domain step Δt (also called learning rate).
- Step 2 Solve Equation (2.11) forward in time and obtain particles $\{\theta_i^n\}_{i=1}^N$ where $\theta_i^n \approx \theta_i(n\Delta t)$ at any fixed $n \in \mathbb{N}$. The obtained empirical measure

$$\frac{1}{N} \sum_{i=1}^N \delta_{\theta_i^n}(\theta)$$

approximates the PDE solution $\rho_\theta(\theta, n\Delta t)$ in the distributional sense, subject to numerical error, random error and potential (density) estimation error.

2.5. Implementation Details. There are a few key terms in the forward operator evaluation (2.3) and the particle formulation (2.11) that require careful attention.

2.5.1. The Fréchet Derivative. The term $\frac{\delta D}{\delta \rho_y} = \frac{\delta D(\rho_y, \rho_y^\delta)}{\delta \rho_y}$ is the Fréchet derivative of the discrepancy D appearing in (2.6) with respect to ρ_y . Different choices of D to quantify the difference between probability distributions lead to different concrete forms of $\frac{\delta D}{\delta \rho_y}$:

- D is the KL-divergence:

$$\frac{\delta D}{\delta \rho_y}(y) = \log \frac{\rho_y}{\rho_y^\delta}(y) + 1.$$

- D is the squared MMD with a positive definite kernel $k(x, y)$, i.e.,

$$D(\rho_y, \rho_y^\delta) = \int V(y) d\rho_y(y) + \frac{1}{2} \int k(y, y') d\rho_y(y) d\rho_y(y') + C$$

with $V(x) = -\int k(x, y) d\rho_y^\delta(y)$ and $C = \frac{1}{2} \int k(x, y) d\rho_y^\delta(x) d\rho_y^\delta(y)$. The Fréchet derivative then becomes

$$\frac{\delta D}{\delta \rho_y}(y) = \int k(y, y') d\rho_y(y') - \int k(y, y') d\rho_y^\delta(y').$$

One significant benefit of MMD over the KL divergence is the fact that *one does not need density estimation* if ρ_y^δ and ρ_y are supplied in terms of particles. Indeed, if $\rho_y = \frac{1}{N} \sum_{i=1}^N \delta_{y_i}(y)$, $\rho_y^\delta = \frac{1}{M} \sum_{j=1}^M \delta_{y_j^*}(y)$, we may use the following approximation:

$$\begin{aligned} D(\rho_y, \rho_y^\delta) &\approx \frac{1}{2N^2} \sum_{i \neq i'}^N k(y_i, y_{i'}) + \frac{1}{2M^2} \sum_{j \neq j'}^M k(y_j^*, y_{j'}^*) - \frac{1}{NM} \sum_i^N \sum_j^M k(y_i, y_j^*) \\ \frac{\delta D}{\delta \rho_y}(y) &\approx \frac{1}{N} \sum_{i=1}^N k(y, y_i) - \frac{1}{M} \sum_{j=1}^M k(y, y_j^*). \end{aligned}$$

2.5.2. The Adjoint Operator. The term ∇T_ω^\top is the adjoint of the Jacobian ∇T_ω . Even if it is not given explicitly, there are many fast ways to evaluate ∇T_ω^\top . Notable examples include automatic differentiation in neural network training, and adjoint-state method in PDE-constrained optimization. The fundamental reason that one can obtain fast adjoint Jacobian evaluation without obtaining the full Jacobian is that we only need its action along one particular vector direction, which is $\nabla_y \frac{\delta D}{\delta \rho_y}(T_\omega(\theta(t)))$ according to (2.10). To compute this efficiently, we use the `jax.vjp` function from the JAX Python library [4]. This call evaluates the product $\nabla T_\omega^\top \nabla_y \frac{\delta D}{\delta \rho_y}(T_\omega(\theta(t)))$ directly, using reverse-mode autodiff, without ever forming or storing the full Jacobian matrix.

2.5.3. Integration With Respect To μ_ω . Note that in both the forward map (2.3) and the particle method for gradient descent (2.11), we require integration with respect to μ_ω , the law of known random parameter ω . This is a key difference between our cryo-EM-based SIP and those studied in [6, 33]. This additional integration operation could increase the sampling and computational costs by using the Monte Carlo method or other numerical quadrature rules. For example,

$$-\int \nabla T_\omega^\top \nabla_y \frac{\delta D}{\delta \rho_y}(T_\omega(\theta_i)) d\mu_\omega(\hat{\omega}) \approx -\frac{1}{K} \sum_{k=1}^K \nabla T_{\hat{\omega}_{ik}}^\top \nabla_y \frac{\delta D}{\delta \rho_y}(T_{\hat{\omega}_{ik}}(\theta)),$$

which implies that for each particle θ_i , we additionally require K samples $\{\hat{\omega}_{ki}\}_{k=1}^K$, as well as K evaluations of ∇T_ω^\top and $T_\omega(\theta)$. To improve computational efficiency, we explore several sampling strategies to manage the integration with respect to μ_ω .

After applying the forward Euler scheme in time for (2.10), multiplying both sides by

an arbitrary test function $\phi(\theta) : \Theta \rightarrow \mathbb{R}$, and integrate over Θ , we obtain

$$\begin{aligned} \int \phi(\hat{\theta}) d\rho(\hat{\theta}, t_{n+1}) &= \int \phi(\hat{\theta}) d\rho(\hat{\theta}, t_n) - \Delta t \int \nabla_{\hat{\theta}} \phi \cdot \int R(\hat{\theta}, \hat{\omega}) d\rho(\hat{\theta}, t_n) d\mu_{\omega}(\hat{\omega}) \\ &= \iint \left(\phi - \Delta t \nabla_{\hat{\theta}} \phi \cdot R(\hat{\theta}, \hat{\omega}) \right) d\rho(\hat{\theta}, t_n) d\mu_{\omega}(\hat{\omega}) \\ &= \iint \varphi(\hat{\theta}, \hat{\omega}) d\rho(\hat{\theta}, t_n) d\mu_{\omega}(\hat{\omega}), \end{aligned}$$

where

$$(2.12) \quad R(\hat{\theta}, \hat{\omega}) := \nabla_{\hat{\theta}} T_{\hat{\omega}}^{\top} \nabla_y \frac{\delta D}{\delta \rho_y}(T_{\hat{\omega}}(\hat{\theta}))$$

and $\varphi(\hat{\theta}, \hat{\omega}) := \phi - \Delta t \nabla_{\hat{\theta}} \phi \cdot R(\hat{\theta}, \hat{\omega})$. Similarly, multiplying the forward operator (2.3) both sides by an arbitrary test function $\psi : Y \rightarrow \mathbb{R}$ and integrating over Y , we have

$$\begin{aligned} \int \psi(y) \rho_y dy &= \iint \psi(y) d(T_{\hat{\omega}} \# \rho_{\theta})(y) dy d\mu_{\omega}(\hat{\omega}) \\ &= \iint \psi(T_{\hat{\omega}}(\hat{\theta})) d\rho_{\theta}(\hat{\theta}) d\mu_{\omega}(\hat{\omega}) \\ &= \iint \tilde{\varphi}(\hat{\theta}, \hat{\omega}) d\rho_{\theta}(\hat{\theta}) d\mu_{\omega}(\hat{\omega}), \end{aligned}$$

where $\tilde{\varphi}(\hat{\theta}, \hat{\omega}) := \psi(T_{\hat{\omega}}(\hat{\theta}))$. Therefore, both evaluating the forward operator according (2.3) and updating the gradient based on (2.11) can be seen as sampling from a joint distribution $\rho_{\theta} \otimes \mu_{\omega}$ of two independent random variables. (Recall we assume that the law of random variable ω is independent of the parameter distribution.)

There are multiple ways of approximating the expectation of a general φ under the distribution $\rho_{\theta} \otimes \mu_{\omega}$ based on the Monte Carlo method. To illustrate how the choice of sampling scheme can affect the error, we consider three possibilities.

$$I = \iint \varphi(\hat{\theta}, \hat{\omega}) d\mu_{\omega}(\hat{\omega}) d\rho_{\theta}(\hat{\theta})$$

$$(2.13) \quad \overset{\#1}{\approx} \frac{1}{N} \sum_{i=1}^N \varphi(\hat{\theta}_i, \hat{\omega}_i) =: \hat{I}_1, \quad \{(\hat{\theta}_i, \hat{\omega}_i)\} \overset{\text{i.i.d.}}{\sim} \rho_{\hat{\theta}} \otimes \mu_{\omega}$$

$$(2.14) \quad \overset{\#2}{\approx} \frac{1}{N} \frac{1}{K} \sum_{i=1}^N \sum_{k=1}^K \varphi(\hat{\theta}_i, \hat{\omega}_k) =: \hat{I}_2, \quad \{\hat{\theta}_i\} \overset{\text{i.i.d.}}{\sim} \rho_{\theta} \quad \{\hat{\omega}_k\} \overset{\text{i.i.d.}}{\sim} \mu_{\omega},$$

$$(2.15) \quad \overset{\#3}{\approx} \frac{1}{N} \frac{1}{K} \sum_{i=1}^N \sum_{k=1}^K \varphi(\hat{\theta}_i, \hat{\omega}_{ik}) =: \hat{I}_3, \quad \{\hat{\theta}_i\} \overset{\text{i.i.d.}}{\sim} \rho_{\theta} \quad \{\hat{\omega}_{ik}\} \overset{\text{i.i.d.}}{\sim} \mu_{\omega}.$$

In Method 1 given in (2.13), we sample from the joint law $\rho_{\theta} \otimes \mu_{\omega}$, requiring N samples of both the structure and noise parameters. In Method 2 presented in (2.14), all $\hat{\theta}_i$'s share the same set of samples $\{\hat{\omega}_k\}_{k=1}^K \sim \mu_{\omega}$, requiring N sampled structure parameters and K sampled noise parameters.. In Method 3 detailed in (2.15), every parameter sample $\hat{\theta}_i$ has its own set of samples $\{\hat{\omega}_{ik}\}_{k=1}^K$ from μ_{ω} , requiring N sampled structure parameters and NK sampled noise parameters.

To analyze the difference among these choices, we make the simplifying assumption that all three methods provide an unbiased estimation, satisfying $\mathbb{E}[\hat{I}_1] = \mathbb{E}[\hat{I}_2] = \mathbb{E}[\hat{I}_3] = I$. The

variances of the estimators \hat{I}_1 , \hat{I}_2 and \hat{I}_3 are the following:

$$\begin{aligned}\text{Var}[\hat{I}_1] &= \frac{1}{N} \text{Var}_{(\hat{\theta}, \hat{\omega}) \sim \rho_\theta \otimes \mu_\omega} [\varphi(\hat{\theta}, \hat{\omega})], \\ \text{Var}[\hat{I}_2] &= \frac{1}{NK} \text{Var}_{(\hat{\theta}, \hat{\omega}) \sim \rho_\theta \otimes \mu_\omega} [\varphi(\hat{\theta}, \hat{\omega})] + \left(\frac{1}{N} - \frac{1}{NK} \right) \text{Var}_{\hat{\theta} \sim \rho_\theta} \left[\mathbb{E}_{\hat{\omega} \sim \mu_\omega} [\varphi(\hat{\theta}, \hat{\omega})] \right] \\ &\quad + \left(\frac{1}{K} - \frac{1}{NK} \right) \text{Var}_{\hat{\omega} \sim \mu_\omega} \left[\mathbb{E}_{\hat{\theta} \sim \rho_\theta} [\varphi(\hat{\theta}, \hat{\omega})] \right], \\ \text{Var}[\hat{I}_3] &= \frac{1}{NK} \mathbb{E}_{\hat{\theta} \sim \rho_\theta} \left[\text{Var}_{\hat{\omega} \sim \mu_\omega} [\varphi(\hat{\theta}, \hat{\omega})] \right] + \frac{1}{N} \text{Var}_{\hat{\theta} \sim \rho_\theta} \left[\mathbb{E}_{\hat{\omega} \sim \mu_\omega} [\varphi(\hat{\theta}, \hat{\omega})] \right].\end{aligned}$$

Precisely which estimator is the most computationally efficient will depend on the relative cost of drawing samples of $\hat{\omega}$ and $\hat{\theta}$ and the details of φ . If sampling both random variables requires the same computational effort, Method 1 will behave well. In contrast, if $\hat{\omega}$ is easy to sample and φ can be easily re-evaluated for multiple values of $\hat{\omega}$, then Methods 2 and 3 may give improved performance. We leave a more exhaustive exploration of these trade-offs for future work on cryo-EM methods.

In this work we adopt Method 1 in (2.13) for simplicity, specifically using Equation (2.16) for forward evaluation and Equation (2.17) for approximating the gradient dynamics:

$$(2.16) \quad \rho_y \approx \frac{1}{N} \sum_{i=1}^N \delta_{y_i}, \quad y_i = T_{\hat{\omega}_i}(\hat{\theta}_i), \quad \{\hat{\omega}_i\}_{i=1}^N \stackrel{\text{i.i.d.}}{\sim} \mu_\omega, \quad \{\hat{\theta}_i\}_{i=1}^N \stackrel{\text{i.i.d.}}{\sim} \rho_\theta$$

$$(2.17) \quad \rho_\theta^{n+1} \approx \frac{1}{N} \sum_{i=1}^N \delta_{\hat{\theta}_i^{n+1}}, \quad \hat{\theta}_i^{n+1} = \hat{\theta}_i^n - \Delta t R(\hat{\theta}_i^n, \hat{\omega}_i), \quad \{\hat{\omega}_i\}_{i=1}^N \stackrel{\text{i.i.d.}}{\sim} \mu_\omega, \quad \{\hat{\theta}_i^n\}_{i=1}^N \stackrel{\text{i.i.d.}}{\sim} \rho_\theta^n$$

where $R(\hat{\theta}, \hat{\omega})$ is defined in (2.12), and ρ_θ^n is the short-hand notation for $\rho_\theta(\theta, n\Delta t)$.

3. Optimize-Then-Discretize (OTD) and Discretize-Then-Optimize (DTO) Approaches. When it comes to optimization problems over the infinite-dimensional spaces, such as PDE-constrained optimization problems derived from optimal control and inverse problems and the SIP for cryo-EM considered in this work, there are always two approaches to derive gradient formula and perform optimization computationally: optimize then discretize (OTD) and discretize then optimize (DTO).

In OTD approaches, such as the ones we have presented so far, we derive the continuous optimality conditions first and then discretize to construct a numerical scheme. This preserves the analytical properties of the original problem, including symmetries and suitable function spaces. It can also lead to solutions that are more accurate and amenable to mathematical analysis [24, 7, 1].

Moreover, employing the rich geometry of the space of probability measures gives a straightforward route to devising novel algorithms. However, depending on the geometries used, new OTD algorithms may be difficult to discretize. For example, in (2.10), density estimation is needed to obtain ρ_y^δ and ρ_y if one uses the f -divergence as D in (2.6) to quantify the data discrepancy. This issue can be mitigated if one uses the MMD as D instead. Moreover, our gradient descent algorithm (2.11) based on the gradient flow equation (2.10) may not be numerically consistent with the forward map evaluation (2.3) unless careful attention has been paid to the discretization of both (2.3) and (2.10).

In contrast, the DTO approach first starts by directly discretizing the continuous problem and then solving the resulting finite-dimensional optimization problem. DTO schemes may suffer from a lack of convergence theory when the dimension of the parameterized unknown approaches infinity and an inconsistency with the original infinite-dimensional optimization problem. Nevertheless, they are often easy to derive, allowing the use of various numerical optimization techniques. To help make the DTO approach concrete, we give an example below and use it to re-derive a popular data analysis algorithm for cryo-EM data.

3.1. Connection with Maximum A Posterior (MAP) Approaches. Maximum a posteriori (MAP) estimation is one of the most widely used methods for analyzing cryo-EM data [39]. Approaches based on MAP estimation, which form the basis of software such as RELION [29, 40] and cryoSPARC [37], are typically justified by recourse to likelihood-based or Bayesian models. Here, we show that the objective function used by these methods, e.g., [29, Eqn. (2)], can instead be derived by the DTO approach applied to a variational objective with respect to ρ_θ .

To begin, we will attempt to optimize ρ_θ by minimizing the KL divergence between the predicted and observed data distribution with an added regularization term.

$$(3.1) \quad \mathcal{L}(\rho_\theta) = D_{\text{KL}}(\rho_y^\delta || \rho_y) - \lambda \mathbb{E}_{\rho_\theta} [\log \rho_p] = \int \log \frac{\rho_y^\delta}{\rho_y}(y) d\rho_y^\delta(y) - \lambda \int \log \rho_p(\hat{\theta}) d\rho_\theta(\hat{\theta}),$$

where ρ_p is our prior guess for the probability density of θ . To derive an expression for $\rho(y)$, we assume a specific image formation model. We parameterize each structure by the electrostatic potential it exerts in three-dimensional space. For concreteness, let θ lie in a finite-dimensional subspace of $L^2(\mathbb{R}^3)$, and for simplicity, we will refer to θ as a vector.

Under this model, the law of y , denoted by ρ_y , can be written as

$$(3.2) \quad \rho_y = F(\rho_\theta) = \int T_{\hat{\theta} \# \mu_\omega} d\rho_\theta(\hat{\theta}) = \frac{1}{(\sqrt{2\pi}\sigma)^{d_y}} \iint \exp\left(-\frac{|y - H^{\widehat{\omega}_r} \hat{\theta}|^2}{2\sigma^2}\right) d\rho_{\omega_r}(\widehat{\omega}_r) d\rho_\theta(\hat{\theta}),$$

based on the cryo-EM forward operator (2.1). Here, d_y is the dimension of y . Plugging (3.2) into (3.1) and dropping the constant independent of ρ_θ , we have an equivalent objective functional

$$(3.3) \quad \mathcal{L}(\rho_\theta) = - \int \log \left(\iint \exp\left(-\frac{|y - H^{\widehat{\omega}_r} \hat{\theta}|^2}{2\sigma^2}\right) d\rho_{\omega_r}(\widehat{\omega}_r) d\rho_\theta(\hat{\theta}) \right) d\rho_y^\delta - \lambda \int \log \rho_p(\hat{\theta}) d\rho_\theta(\hat{\theta}).$$

Often, we observe the reference data distribution ρ_y^δ through finitely many samples, i.e., $\rho_y^\delta \approx \frac{1}{N} \sum_{i=1}^N \delta_{y_i}$. Then (3.3) reduces to

$$(3.4) \quad \mathcal{L}_N(\rho_\theta) = -\frac{1}{N} \sum_{i=1}^N \log \left(\iint \exp\left(-\frac{|y_i - H^{\widehat{\omega}_r} \hat{\theta}|^2}{2\sigma^2}\right) d\rho_{\omega_r}(\widehat{\omega}_r) d\rho_\theta(\hat{\theta}) \right) - \lambda \int \log \rho_p(\hat{\theta}) d\rho_\theta(\hat{\theta}).$$

Note that $\mathcal{L}_N(\rho_\theta) \xrightarrow{N \rightarrow \infty} \mathcal{L}(\rho_\theta)$ almost surely for any fixed ρ_θ if the strong law of large number (SLLN) holds. Furthermore, we can also approximate ρ_θ by an empirical measure, $\rho_\theta \approx \frac{1}{K} \sum_{k=1}^K \delta_{\theta_k}$. Then the discretized \mathcal{L}_N under this particular parameter distribution approximation becomes (again after dropping the constant)

$$(3.5) \quad \mathcal{L}_{N,K}(\theta) = -\frac{1}{N} \sum_{i=1}^N \log \left(\sum_{k=1}^K \int \exp\left(-\frac{|y_i - H^{\widehat{\omega}_r} \theta_k|^2}{2\sigma^2}\right) d\rho_{\omega_r}(\widehat{\omega}_r) \right) - \frac{\lambda}{K} \sum_{k=1}^K \log \rho_p(\theta_k),$$

where $\theta = (\theta_1, \dots, \theta_K)$. We remark that (3.5) is precisely [29, Eqn. (2)] with $\lambda = \frac{K}{N}$ and up to a normalizing constant $\frac{1}{N}$.

3.2. Large Data Limit for DTO Schemes. An important property essential for both OTD and DTO frameworks is consistency. That is, as the discretization scheme refines, the minimizer of the discretized problem converges to that of the continuous variational problem. For the OTD framework, consistency is easier to ensure since the continuous problem's optimality condition is first derived, and discretization applies to solve for the minimizer from the optimality condition. The error incurred can often be analyzed by numerical analysis.

On the other hand, convergence of the minimizers for the DTO framework is not so trivial since the variational problem of interests in DTO is fundamentally different from the one of the continuous problem, e.g., in a finite-dimensional search space (see Equation (3.5)) versus an infinite-dimensional search space (see Equation (3.1)). Consequently, while our focus remains on OTD schemes, given the prior use of DTO approaches in cryo-EM, we give a few conditions such that a DTO framework formulated for the cryo-EM problem is consistent with the continuous problem.

Recall the objective functional $E(\rho_\theta) = D(F(\rho_\theta), \rho_y^\delta)$ in (2.6) where D is a certain divergence or metric over the space of probability distributions. Define

$$E_N = D\left(F(\rho_\theta), \frac{1}{N} \sum_{i=1}^N \delta_{y_i}\right)$$

where $\{y_i\}_{i=1}^N$ are samples of ρ_y^δ ; see (3.4) for an example. One may work with E_N rather than E due to either a limited access to the reference data distribution ρ_y^δ or discretization of the functional. We then have two variational problems:

$$(3.6) \quad \inf_{\rho_\theta \in \Omega \subset \mathcal{P}(\Theta)} E(\rho_\theta),$$

$$(3.7) \quad \inf_{\rho_\theta \in \Omega \subset \mathcal{P}(\Theta)} E_N(\rho_\theta).$$

The convergence of (3.7) to (3.6) can be established through Γ -convergence [5].

PROPOSITION 3.1. *Consider a Polish space $(\mathcal{P}(\Theta), W_2)$. Assume that*

A1 *$D(\mu, \nu)$ is jointly lower semi-continuous in (μ, ν) with respect to the $(\mathcal{P}(Y), W_2)$ topology where $F(\Theta) \subseteq Y$, and*

A2 *$\forall \lambda \in \mathbb{R}, \exists K_\lambda \subset \Omega$ compact such that $\{\rho_\theta \in \Omega : E_N(\rho_\theta) \leq \lambda\} \subset K_\lambda$ for all N , and*

A3 *$E_N(\rho_\theta) \xrightarrow{N \rightarrow \infty} E(\rho_\theta)$ almost surely for any $\rho_\theta \in \Omega$.*

Then the following equation holds almost surely

$$(3.8) \quad \min_{\rho_\theta \in \Omega \subset \mathcal{P}(\Theta)} E(\rho_\theta) = \lim_{N \rightarrow \infty} \min_{\rho_\theta \in \Omega \subset \mathcal{P}(\Theta)} E_N(\rho_\theta).$$

Proof. First, note that the forward map (3.2) based on (2.1) is a linear push-forward map with a bounded Lipschitz constant. We have

$$(3.9) \quad W_2(F(\rho_\theta), F(\rho'_\theta)) \leq CW_2(\rho_\theta, \rho'_\theta).$$

Consequently, given any converging sequence $\{\rho_\theta^j\}_{j=1}^\infty \subset \Omega$ to ρ_θ , we obtain a converging sequence $\{\rho_y^j\}_{j=1}^\infty \subset Y$ to $\rho_y = F(\rho_\theta)$. By Assumption **A1**,

$$D(F(\rho_\theta), \nu) = D(\rho_y, \nu) \leq \liminf_j D(\rho_y^j, \nu) = \liminf_j D(F(\rho_\theta^j), \nu),$$

for any ν . When $\nu = \rho_y^\delta$ and $\nu = \frac{1}{N} \sum_{i=1}^N \delta_{y_i}$, we obtain that E and E_N are lower semi-continuous, respectively. Since Assumption **A2** implies the coercivity of E_N , together with the lower semi-continuity of E_N , $\forall N$, we know minimizers exist for the sequence of variational problems given in (3.7).

Next, we verify the Γ -convergence of E_N to E . First, for every sequence $\{\rho_\theta^N\}_{N=1}^\infty$ converging to ρ_θ , we have also $\{\rho_y^N\}_{N=1}^\infty$ converging to ρ_y as a result of (3.9) where $\rho_y^N = F(\rho_\theta^N)$ and $\rho_y = F(\rho_\theta)$. Since $E_N(\rho_\theta^N) = D(\rho_y^N, \hat{\rho}_y^N)$ where $\hat{\rho}_y^N := \frac{1}{N} \sum_{i=1}^N \delta_{y_i}$, $\{\rho_y^N\}_N \xrightarrow{N \rightarrow \infty} \rho_y$ and the empirical measure $\{\hat{\rho}_y^N\}_N \xrightarrow{N \rightarrow \infty} \rho_y^\delta$ almost surely [17, Thm. 11.4], we have

$$E(\rho_\theta) = D(\rho_y, \rho_y^\delta) \leq \liminf_N D(\rho_y^N, \hat{\rho}_y^N) = \liminf_N E_N(\rho_\theta^N)$$

as a result of the joint lower semi-continuity by **A1**. So far, we have verified the ‘‘liminf’’ condition of the Γ convergence. The ‘‘existence of a recovery sequence’’ directly holds because of Assumption **A3**, which is equivalent to SLLN. Hence, $\{E_N\}_N$ Γ -converges to E .

Finally, by the Fundamental Theorem of Γ -convergence [5, Thm. 2.10], we get (3.8). \square

Next, we study the convergence in terms of the particle discretization of the parameter distribution ρ_θ . Recall $\mathcal{P}(\Theta)$ in (2.6) represents the space of probability measures over Θ . Without loss of generality, we assume that the search domain $\Omega = \mathcal{P}(\Theta)$. We denote the set of all empirical measures in $\mathcal{P}(\Theta)$ by

$$\mathcal{P}_{\text{em}}(\Theta) = \left\{ \rho_\theta := \frac{1}{K} \sum_{k=1}^K \delta_{\theta_k} : \theta_1, \dots, \theta_K \in \Theta, \forall K \in \mathbb{N} \right\},$$

and the set of empirical measures consisting of K particles by

$$\mathcal{P}_{\text{em}}^K(\Theta) = \left\{ \rho_\theta := \frac{1}{K} \sum_{k=1}^K \delta_{\theta_k} : \theta_1, \dots, \theta_K \in \Theta \right\}.$$

LEMMA 3.2. *Consider an objective functional $E : \mathcal{P}(\Theta) \rightarrow \mathbb{R}$ that maps a probability distribution ρ_θ to a real number. Assume E is continuous in ρ_θ with respect to the weak topology, and both variational problems*

$$\inf_{\rho_\theta \in \mathcal{P}(\Theta)} E(\rho_\theta), \quad \inf_{\rho_\theta \in \mathcal{P}_{\text{em}}^K(\Theta)} E(\rho_\theta)$$

admit minimizers, $\forall K \in \mathbb{N}$. We then have

$$\lim_{K \rightarrow \infty} E(\rho_\theta^K) = E(\rho_\theta^*),$$

where $\rho_\theta^K \in \arg \min_{\rho_\theta \in \mathcal{P}_{\text{em}}^K(\Theta)} E(\rho_\theta)$, and $\rho_\theta^* \in \arg \min_{\rho_\theta \in \mathcal{P}(\Theta)} E(\rho_\theta)$.

Proof. Since $\mathcal{P}_{\text{em}}(\Theta)$ is dense in $\mathcal{P}(\Theta)$ with respect to the weak topology, we have the following due to the continuity of E :

$$\inf_{\rho_\theta \in \mathcal{P}_{\text{em}}(\Theta)} E(\rho_\theta) = \inf_{\rho_\theta \in \mathcal{P}(\Theta)} E(\rho_\theta).$$

Next, we prove that

$$(3.10) \quad \lim_{K \rightarrow \infty} \min_{\rho_\theta \in \mathcal{P}_{\text{em}}^K(\Theta)} E(\rho_\theta) = \inf_{\rho_\theta \in \mathcal{P}_{\text{em}}(\Theta)} E(\rho_\theta).$$

For convenience, we use the short-hand notations: $A_K = \min_{\rho_\theta \in \mathcal{P}_{\text{em}}^K(\Theta)} E(\rho_\theta)$ and $B = \inf_{\rho_\theta \in \mathcal{P}_{\text{em}}(\Theta)} E(\rho_\theta)$. Since $\mathcal{P}_{\text{em}}^K(\Theta) \subset \mathcal{P}_{\text{em}}$ for any K , we have $A_K \geq B$ and thus

$$(3.11) \quad \liminf_{K \rightarrow \infty} A_K \geq B.$$

On the other hand, based on the property of infimum, for any $\epsilon > 0$, there exists $K(\epsilon) \in \mathbb{N}$ such that

$$A_{K(\epsilon)} \leq E(\rho_\theta^{K(\epsilon)}) < B + \frac{\epsilon}{2}.$$

For the given ϵ and this probability measure $\rho_\theta^{K(\epsilon)} \in \mathcal{P}_{\text{em}}^{K(\epsilon)}(\Theta)$, there exists $M(\epsilon) \in \mathbb{N}$ such that whenever $N \geq M(\epsilon)$, the best N -particle empirical measure approximation of $\rho_\theta^{K(\epsilon)}$ in the set $\mathcal{P}_{\text{em}}^N$, denoted by ρ^N , is close to $\rho_\theta^{K(\epsilon)}$ such that

$$\left| E(\rho_\theta^{K(\epsilon)}) - E(\rho^N) \right| \leq \frac{\epsilon}{2}.$$

Here, we use the assumption that E is continuous in the weak topology. This leads to

$$A_N = \min_{\rho_\theta \in \mathcal{P}_{\text{em}}^N(\Theta)} E(\rho_\theta) \leq E(\rho^N) \leq E(\rho_\theta^{K(\epsilon)}) + \frac{\epsilon}{2} \leq B + \epsilon,$$

for any $N > M(\epsilon)$. Based on the arbitrariness of ϵ , we then have $\limsup_{N \rightarrow \infty} A_N \leq B$. Combining this inequality with (3.11), we obtain (3.10). Putting everything together, we have

$$\lim_{K \rightarrow \infty} E(\rho_\theta^K) = \lim_{K \rightarrow \infty} \min_{\rho_\theta \in \mathcal{P}_{\text{em}}^K(\Theta)} E(\rho_\theta) = \inf_{\rho_\theta \in \mathcal{P}_{\text{em}}(\Theta)} E(\rho_\theta) = \min_{\rho_\theta \in \mathcal{P}(\Theta)} E(\rho_\theta) = E(\rho_\theta^*),$$

which finishes the proof. \square

Note that Lemma 3.2 only states the convergence of the objective functional. To obtain the convergence of the minimizing distributions, we need extra assumptions. The following proposition provides a sufficient condition.

PROPOSITION 3.3. *Let all conditions in Lemma 3.2 hold and the objective functional E have a unique minimizer ρ_θ^* . Suppose E satisfies an Lojasiewicz-type inequality at ρ_θ^* :*

$$(3.12) \quad d(\nu, \rho_\theta^*) \leq C|E(\nu) - E(\rho_\theta^*)|^\alpha, \quad \forall \nu \in \mathcal{P}(\Theta),$$

for some constants $C, \alpha > 0$, where $d(\nu, \rho_\theta^*)$ is some divergence or metric over $\mathcal{P}(\Theta)$. Then

$$\lim_{K \rightarrow \infty} d(\rho_\theta^K, \rho_\theta^*) = 0.$$

Proof. The result is a direct consequence of (3.12) and Lemma 3.2. \square

4. Numerical Examples. To demonstrate the use of gradient flows for cryo-EM, we present three progressively more complex examples using the proposed particle method (2.11) on simulated cryo-EM data. Throughout the section, we use the KL divergence (2.7) and the MMD (2.8) (including the energy distance (2.9)) as objective functions along with the Wasserstein metric to determine the geometry. Therefore, the gradient expression reduces to Equation (2.10). In contrast to the MAP approaches discussed in Subsection 3.1, we do not apply algorithms that assume a specific reconstruction algorithm *a priori*.

Algorithm 4.1 Gradient descent with image matching and Jacobian-vector products

Input: Observed images y^δ , initial modes $\theta^0 = \{\theta_j^0\}_{j=1}^M$, noise level σ , imaging parameters, protein parameters, learning rate vector η

Output: Optimized latent variables θ^{final}

for iteration $l = 0, 1, 2, \dots, N_{\text{max}}$ **do**

 Generate random noise $\{\hat{\omega}_{n_j}\}_{j=1}^N$ from $\mathcal{N}(0, \sigma^2 I)$

 Generate random orientations $\{\hat{\omega}_{r_j}\}_{j=1}^N$ from uniform quaternion distribution

 Set $y_j^l = T_{\hat{\omega}_j}(\theta_j^l)$ with $\hat{\omega}_j = (\hat{\omega}_{n_j}, \hat{\omega}_{r_j})$ for $j = 1, \dots, N$

 Compute $\frac{d}{dt}\theta_j(t)$ according to Equation (2.11)

 Update θ_j using Adam: $\theta_j^{l+1} \leftarrow \text{Adam}\left(\frac{d}{dt}\theta_j(t), \theta_j^l, \eta\right)$

end for

return $\theta^{\text{final}} = \theta^{\text{maxiter}}$

4.1. One-dimensional Test System. We begin with a simple, low-dimensional example to illustrate the core ideas of our framework. In this setting, the latent space is one-dimensional, and the forward map is the identity perturbed by additive noise. This example serves as an intuitive demonstration of the algorithm’s ability to recover an unknown latent distribution from noisy observations. In particular, this lets us efficiently compare the performance of the method under two different discrepancy measures, the KL divergence and the energy distance, to study the effect of the chosen objective on the final outcome.

We define the forward operator as

$$T_\omega(\theta) = \theta + \omega, \quad \theta \in \mathbb{R} \quad \omega \sim \mathcal{N}(0, \sigma^2),$$

where ω represents additive noise and $\sigma = 1.5$. The true parameters distribution is defined as a mixture of two Gaussians:

$$\theta \sim \frac{1}{2} \cdot \mathcal{N}(-2, 0.75^2) + \frac{1}{2} \cdot \mathcal{N}(2, 0.3^2).$$

The observed data are generated by adding independent noise to the samples:

$$y^\delta = y + \delta, \quad \delta \sim \mathcal{N}(0, \sigma^2).$$

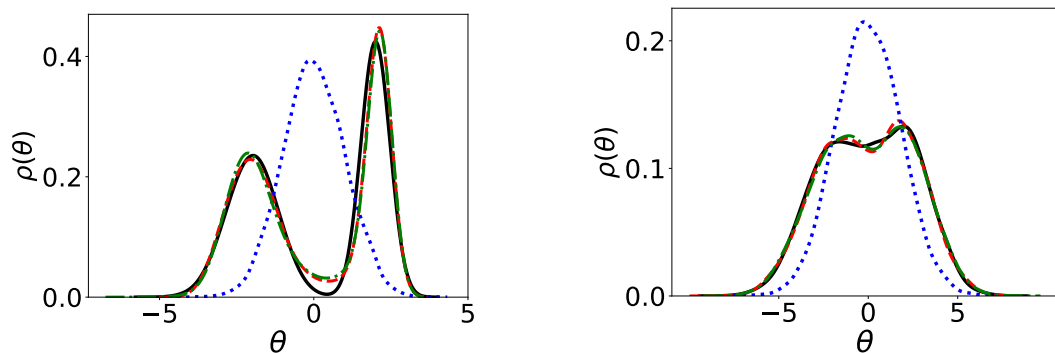
We use $n = 10^4$ observations and perform 25000 optimization iterations of Algorithm 4.1.

As the discrepancy measure, we use the KL divergence and the Energy Distance. For the Energy Distance, the distributions are approximated by Dirac delta functions centered at the particle locations. For the KL divergence, the distributions ρ_θ , ρ_y , and ρ_y^δ , are estimated via kernel density estimation with an isotropic Gaussian kernel [13]:

$$\rho_y^N(y) \approx \frac{1}{N} \sum_{j=1}^N \phi^\epsilon(y - y_j), \quad \phi^\epsilon(y) = \frac{1}{(2\pi\epsilon)^{1/2}} \exp\left(-\frac{y^2}{2\epsilon}\right).$$

For the KL divergence, the bandwidth in the kernel density estimation was determined using Silverman’s rule-of-thumb. Applying this method to our dataset resulted in a bandwidth value of 0.3496. The initial parameter distribution ρ_{θ_0} is set to $\mathcal{N}(0, 1)$, represented by 10^4 i.i.d. samples. We then apply the particle-based algorithm described in Equation (2.11) to approximate the Wasserstein gradient flow (2.10).

Fig. 1 compares the performance of KL divergence and energy distance as objective functions, showing that both lead to nearly identical reconstructions. In both cases, the final estimated distributions closely match the ground truth, demonstrating the method’s effectiveness in this simple example. To quantitatively compare both methods, we employ the Wasserstein distance as the evaluation metric. Using the Energy Distance, the discrepancy between the estimated distribution in parameter space and the ground-truth distribution is 0.1911. When using the KL divergence, this distance is 0.1870, indicating that KL yields a slightly better result.



(a) Parameter distributions (initial, estimated, ground truth) using Energy distance and KL divergence..

(b) Data distributions (initial, estimated, ground truth) using Energy distance and KL divergence.



Fig. 1: One-dimensional Test System: Comparison among true, estimated, and initial distributions under two different loss functions: energy distance and KL divergence. Columns show parameter space (left) and data space (right). The legend indicates line styles for each distribution.

Fig. 2 summarizes the computational effort required to reach a Wasserstein distance below 0.2 for different noise levels σ . Fig. 2a reports the number of iterations needed to reach a Wasserstein distance below 0.2 for different noise levels σ , while Fig. 2b shows the corresponding computation times in minutes. Both methods become more computationally demanding as the noise level increases, but the KL divergence exhibits greater variability with respect to noise. Although KL achieves a slightly smaller final Wasserstein distance, Fig. 2b shows that it requires longer computation times to reach the same accuracy threshold, particularly at higher noise levels. This is mainly because each iteration is more expensive when using KL than when using the Energy Distance, primarily due to the use of kernel density estimation (KDE) in the KL computation. Furthermore, when the noise level is either low or very high, KL also requires more iterations than the Energy Distance, leading to substantially higher total runtime in these regimes. Overall, the Energy Distance appears to be more stable with respect to noise and can be more computationally efficient.

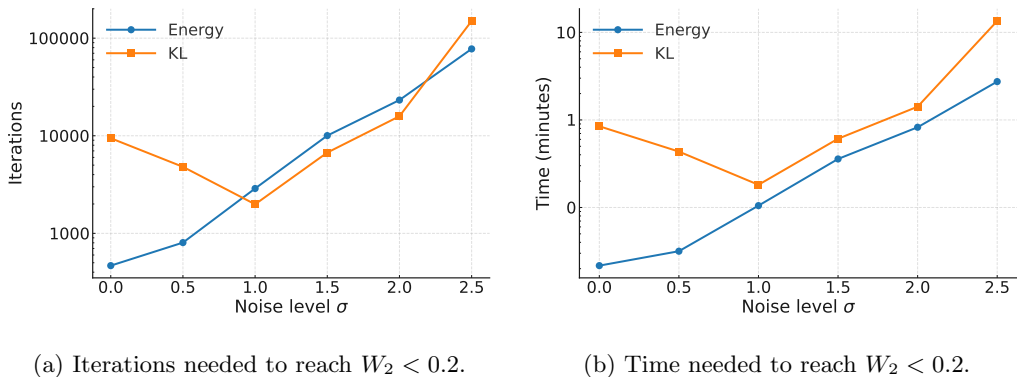


Fig. 2: Comparison of the number of iterations (left) and computation time in minutes (right) required to reach a Wasserstein distance below 0.2 for different noise levels σ , using the Energy Distance (blue circles) and KL divergence (orange squares) as objective functions.

4.2. Heterogeneity in Nanoclusters. To further validate our work, we next apply it to a more realistic system with a nontrivial image formation model. Here, we model the formation of cryo-EM images on a cluster of four particles arranged in a rectangle, imaged from the top. Each arrangement of particles is parameterized by the rectangle’s width and height, giving a two-dimensional latent space

However, the observed images are high-dimensional: each image has 128×128 pixels. Consequently, this example lets us benchmark the performance of our approach for high-dimensional observed data by assessing how well we recover the latent low-dimensional latent distribution.

The deterministic forward map is defined as $T : \mathbb{R}^2 \rightarrow \mathbb{R}^{128 \times 128}$, which transforms a latent variable $\theta \in \mathbb{R}^2$ into a 2D image. The transformation is constructed through a symmetric arrangement of atomic positions. The steps are as follows:

1. Initialize the first atomic position by halving the latent variable: $\mathbf{a}_1 = \frac{\theta}{2}$.
2. Three additional atomic positions are generated by applying axis reflections:

$$\mathbf{a}_2 = \mathbf{a}_1 \odot [1, -1], \quad \mathbf{a}_3 = \mathbf{a}_1 \odot [-1, 1], \quad \mathbf{a}_4 = \mathbf{a}_1 \odot [-1, -1],$$

where \odot denotes the element-wise product.

3. These atomic positions are stacked into a tensor $\mathbf{A} = [\mathbf{a}_1^\top, \mathbf{a}_2^\top, \mathbf{a}_3^\top, \mathbf{a}_4^\top]^\top \in \mathbb{R}^{4 \times 2}$. The rendering process maps the atomic structures into 2D images of size 128×128 . This is achieved by projecting the atomic positions onto a pixel grid and applying a Gaussian kernel to model atomic contributions. The steps are detailed below:

1. **Defining the pixel grid.** A uniformly spaced grid $\mathbf{g} \in \mathbb{R}^{2 \times 128 \times 128}$ is defined over the range $[-4, 4]$ with $\mathbf{g}_{ij} = (-4 + \frac{8i}{128}, -4 + \frac{8j}{128})$, $i, j = 0, \dots, 127$.
2. **Computing squared displacements.** For each atomic position $\mathbf{a}_k \in \mathbf{A}$, we calculate the squared displacement relative to each grid point $\Delta \mathbf{g}_{ijk} = (\mathbf{a}_k - \mathbf{g}_{ij})^2$, and the squared distance is obtained as $d_{ijk}^2 = \sum_{l=1}^2 (\Delta \mathbf{g}_{ijk})_l$.
3. **Applying the Gaussian kernel.** The atomic contributions are modeled using a Gaussian kernel, parameterized by τ : $K_{ijk} = \exp(-d_{ijk}^2/(2\tau^2))$.
4. **Summing contributions.** The final pixel intensity is computed by summing the contributions of all atoms $I_{ij} = \sum_{k=1}^4 K_{ijk}$.

Fig. 3 illustrates the resulting images. Fig. 3a shows examples of noiseless images generated from the structure parameters, while Fig. 3b displays the corresponding noisy observations.

We define the random map as $T_\omega(\theta) = T(\theta) + \omega$, where $\omega \sim \mathcal{N}(0, \sigma^2 \mathbf{I})$ is pixel-wise Gaussian noise. The latent variables θ are sampled from a Gaussian mixture model in \mathbb{R}^2 :

$$\theta \sim \alpha \mathcal{N} \left(\begin{bmatrix} 3 \\ 3 \end{bmatrix}, \begin{bmatrix} 0.5 & 0 \\ 0 & 0.5 \end{bmatrix} \right) + (1 - \alpha) \mathcal{N} \left(\begin{bmatrix} 5 \\ 5 \end{bmatrix}, \begin{bmatrix} 0.7 & 0.5 \\ 0.5 & 1 \end{bmatrix} \right),$$

where $\alpha = 0.2$. The initial guess $\theta_0 \sim \mathcal{N} \left(\begin{bmatrix} 4 \\ 4 \end{bmatrix}, \begin{bmatrix} 0.8 & 0.3 \\ 0.3 & 0.8 \end{bmatrix} \right)$.

Observed images are generated as $y^\delta = T(\theta) + \delta$, with $\delta \sim \mathcal{N}(0, \sigma^2 \mathbf{I})$ and $\sigma = 1.5$. We use $n = 1000$ observations and run Algorithm 4.1 for 3000 iterations. As the objective function, we use the energy distance (2.9), and define the geometry using the W_2 metric.

To estimate the distributions ρ_θ , ρ_y , and ρ_{y^δ} , we approximate the distributions using Dirac delta functions placed at the particle locations. The particle-based gradient flow (2.10) is implemented using the scheme in Equation (2.11).

The convergence results are shown in Fig. 4. We see good results with the underlying reference density: energy distance in parameter space decreases from 0.429 (initial vs true) to 0.0163 (estimated vs true). In image space, it drops from 0.0947 to 0.0277 when comparing the initial and final distributions to the observed data.

Our results suggest that gradient flows are able to recover the latent probability densities even when the observed images are high-dimensional.

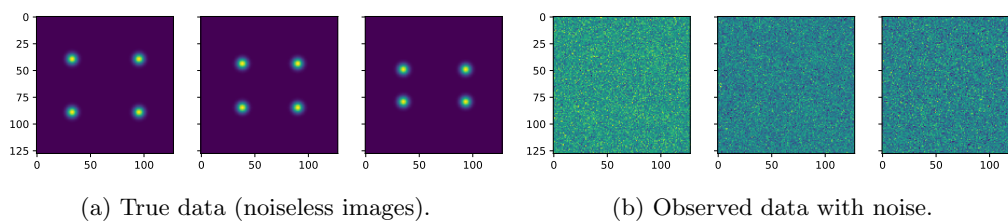


Fig. 3: Heterogeneity in Nanoclusters: Visual comparison between the true images generated from the clean data (a) and the corresponding noisy observations (b).

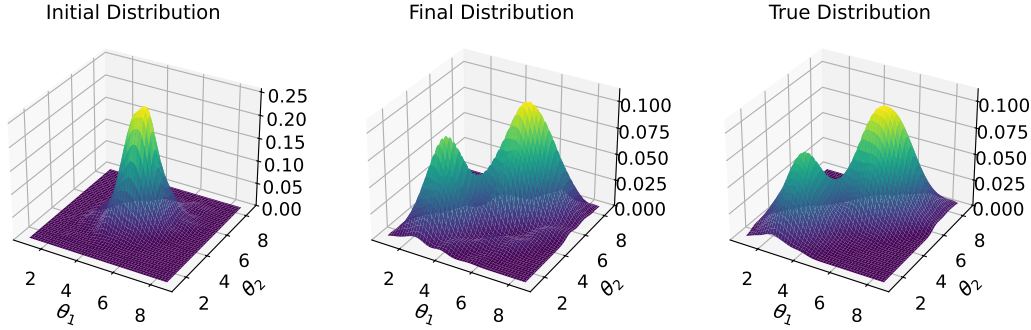


Fig. 4: Heterogeneity in Nanoclusters: The initial parameter distribution (left), the estimated distribution (middle) after optimization and the ground truth distribution (right) are shown.

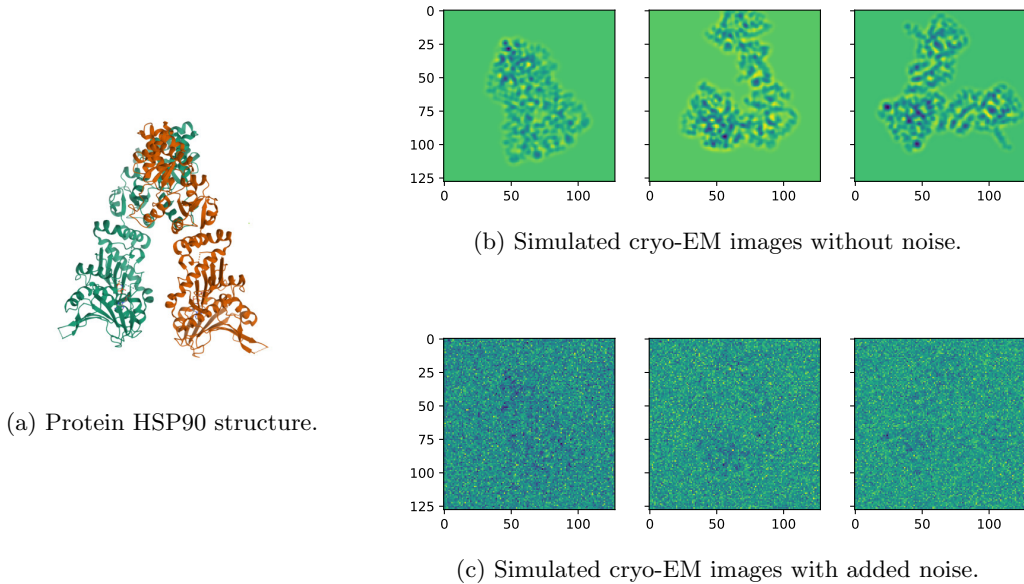


Fig. 5: Illustrations of the 3D structure of protein HSP90 (a) and 2D simulated cryo-EM projections (b) and (c). In particular, (b) shows noiseless projections while (c) includes Gaussian noise to simulate experimental conditions.

4.3. Simulated Protein Cryo-EM. The final example aims to emulate the recovery of conformational heterogeneity on a realistic model for cryo-EM of a flexible protein. Using a standard model of cryo-EM image formation, we simulate realistic images of the HSP90 protein undergoing a conformational change, taken from random rotations. We then attempt to recover this conformational change from the observed images.

Figs. 5a, 5b, and 5c respectively display the 3D molecular structure, the noiseless projections generated from atomic positions, and the noisy observations used as input to the optimization framework.

To model realistic protein conformational changes, we employ a low-dimensional representation of protein dynamics based on normal modes. Normal modes capture the collective, low-frequency vibrations of the protein and are derived by solving the eigenvalue problem of the Hessian matrix associated with the potential energy landscape. The resulting eigenvec-

tors represent directions of motion, while the eigenvalues quantify the stiffness or frequency of these motions. Biologically relevant conformational changes—such as hinge bending or domain opening and closing—are typically encoded in the low-frequency modes associated with the smallest eigenvalues [48, 25, 2]. In this example, we focus on the four principal modes of the protein HSP90, with the initial structure adapted from Protein Data Bank entry 2IOP [42]. These four modes, calculated using the ProDy python package [51], give a compact yet physically meaningful basis for the optimization process. The implementation of protein-to-image mapping was carried out using the cryoJAX library [15].

Combining the cryo-EM image formation model (2.1) with a low-dimensional representation of protein motion via structural modes, the images generated are given by:

$$y = T(\theta, \omega) = H^{\omega_r} G(\theta) + \omega_n,$$

where ω_n denotes the noise term and follows the distribution $\delta \sim \mathcal{N}(\mathbf{0}, \mathbf{I}_{128 \times 128})$, ω_r is the rotation used in the image projection, $\theta = (\theta_1, \theta_2, \theta_3, \theta_4)$ denotes the low-dimensional coordinate vector encoding the protein’s conformational modes and $G: \mathbb{R}^4 \rightarrow \mathbb{R}^{N \times N \times N}$ is the function that maps modes to a 3D electrostatic potential.

For the true distribution over modes ρ_θ^* , we sample θ_1 and θ_2 are sampled from a Gaussian mixture and scaled each mode according to the inverse square root of its eigenvalue $\theta_i = z_i/\sqrt{\lambda_i}$, $z_i \sim \frac{1}{2}\mathcal{N}(9, 1) + \frac{1}{2}\mathcal{N}(-7, 1)$, $i = 1, 2$. The modes θ_3 and θ_4 are sampled from a Gaussian and scaled each mode according to the inverse square root of its eigenvalue $\theta_i = z_i/\sqrt{\lambda_i}$, $z_i \sim \mathcal{N}(0, 1)$, $i = 3, 4$. In contrast, for our initial guess distribution ρ_θ we sample each mode from a uniform distribution and scale the value according to the inverse square root of the corresponding eigenvalue $\theta_{0i} = v_i/\sqrt{\lambda_i}$, $v_i \sim \mathcal{U}(-7, 7)$, $i = 1, 2, 3, 4$ from the normal mode calculation.

The observed images have been generated by $y = T(\theta, \omega = (\omega_r, \delta)) = H^{\omega_r} G(\theta) + \delta$, the noise δ follows the distribution $\delta \sim \mathcal{N}(\mathbf{0}, \mathbf{I}_{128 \times 128})$. We assume that all images are centered, but random rotations are drawn from $R \sim \mathcal{U}(\text{SO}(3))$. We use 3000 images and we perform Algorithm 4.1 for 9×10^4 number of iterations. This is a modest number of images by experimental standards: cryo-EM experiments can collect hundreds of thousands, or millions, of particles [3]. We use the energy distance (2.9) to quantify the discrepancy between the distribution of generated images and the distribution of observed cryo-EM images. We approximate the distributions, $\rho_\theta, \rho_{y^\delta}$ and ρ_y , using Dirac delta functions placed at the particle locations.

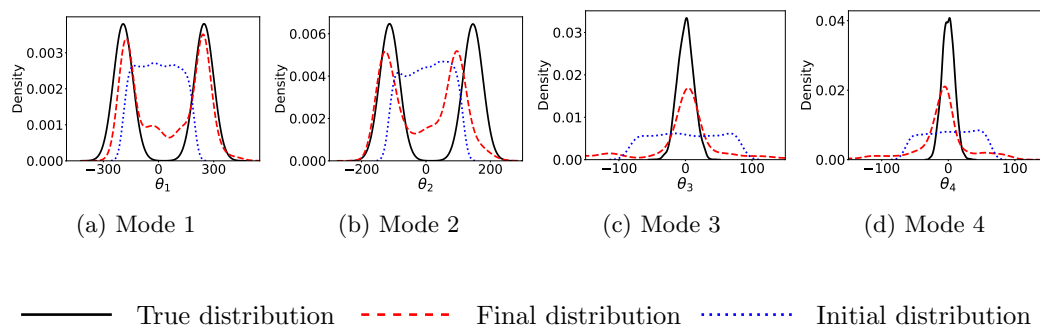


Fig. 6: Cryo-EM synthetic example: Comparison between the true parameter distribution (black), the estimated distribution (red), and the initial guess (blue). From left to right: Mode 1 to Mode 4.

When comparing the marginal resulting distributions, we observe that in all cases there is a reasonably accurate approximation of the true distribution. As illustrated in Fig. 6a, the estimation for the first mode is highly accurate, closely matching the ground truth. The second mode, shown in Fig. 6b, also yields a very good approximation, though slightly

less precise than that of the first. In contrast, as shown in Figs. 6c and 6d, the recovered distributions for the third and fourth modes exhibit more noticeable deviations from the target. This may be attributed to the fact that the first modes describe more prominent and higher-magnitude motions, making them easier to estimate or observe. This difference is particularly noticeable given the stochastic nature of the example.

The energy distance in parameter space decreases from 89.21 (initial vs. true) to 19.44 (estimated vs. true). In image space, it drops from 1.13 to 0.21 when comparing the initial and final distributions to the observed data. These results demonstrate an improvement in both representations.

To visualize the structural motions associated with each mode, we refer the reader to Figs. 7. As illustrated, the deformations corresponding to the last two modes are very subtle and difficult to observe. When stochastic variability is introduced through additive noise, recovering these motions becomes even more challenging. Nevertheless, despite the limited amount of data and the small number of input images, the proposed method is still able to recover the overall shape of the distribution and identify the predominant conformational states.

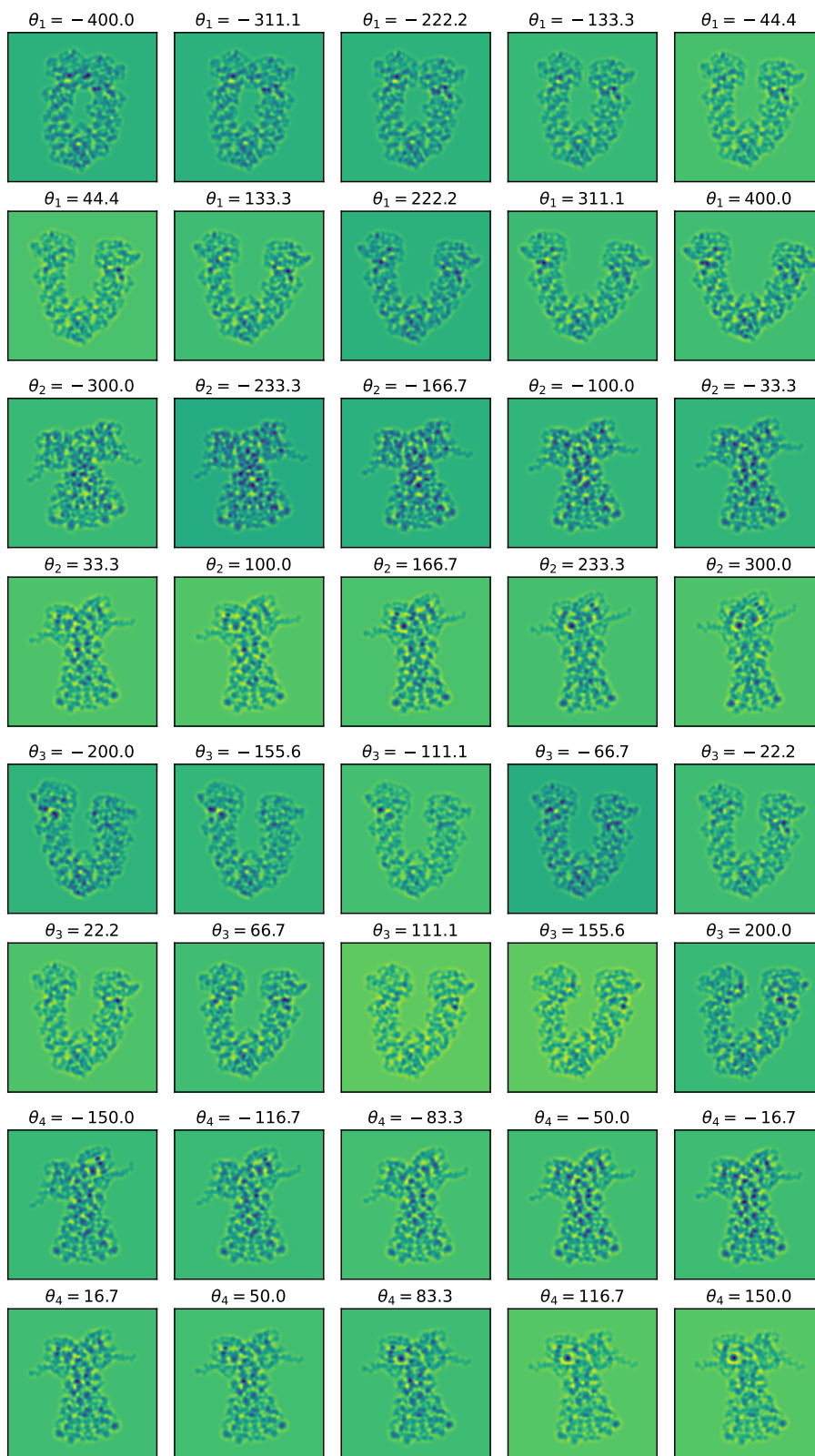


Fig. 7: Visualization of conformational variability along 4 dominant normal modes. Each pair of rows corresponds to a distinct mode, ordered from top to bottom starting with Mode 1 to Mode 4.

To compare the image distributions, we project them onto their first two principal components, denoted β_1 and β_2 , which capture the directions of highest variance in the high-dimensional image space. This projection reduces the dimensionality of the data, enabling meaningful visualization and comparison of the distributions.

To simplify the analysis, we fix the viewing directions throughout the experiment. By removing ambiguity due to random rotations, this setup ensures that variations in the images are primarily due to differences in molecular conformation, rather than orientation. Figs. 8a and 8b show the marginal distributions along β_1 and β_2 for the *noisy images*.

In both directions, we observe that the estimated distribution aligns well with the true distribution, particularly along β_1 , suggesting that the Wasserstein gradient flow effectively captures the main structure of image variability despite the presence of observational noise.

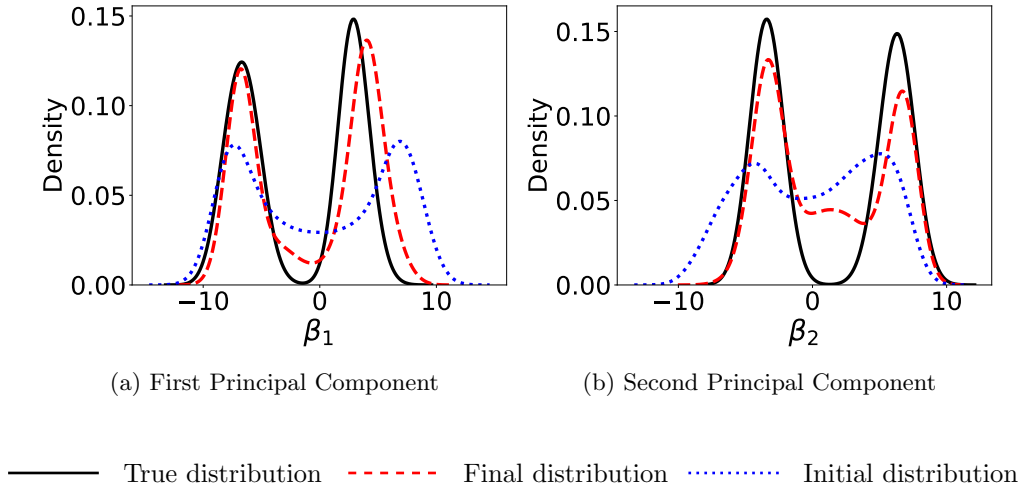


Fig. 8: Cryo-EM Synthetic Example: Comparison among PCA for the true PCA distribution (black), initial PCA distribution (blue) and final PCA distribution (red) of noisy images.

5. Conclusion and Discussions. This work introduces and analyzes a nonparametric framework for cryo-EM reconstruction by formulating the problem as a stochastic inverse problem (SIP) in the space of probability measures. By interpreting cryo-EM image formation as a random push-forward map, the proposed method enables the recovery of an entire distribution over molecular conformations rather than a finite set of discrete states. This perspective allows for a systematic variational formulation of the inverse problem, which is solved using the Wasserstein gradient flow. The gradient flow naturally suggests a particle-based implementation, which allows for scalable and efficient inference over structural distributions, and the method remains robust in the presence of observational noise. Importantly, we can build algorithms that do not require an explicit model for the formation of cryo-EM images. Rather, it is enough to be able to simulate the random image formation process.

To demonstrate our formalism, we apply a specific Wasserstein gradient flow to a series of numerical experiments, building up from a simple one-dimensional example to an experiment with realistic synthetic cryo-EM data. Our results show that we are capable of recovering conformational landscapes and recovering structural variability. While one might worry that recovering additional conformational data would require considerably more data compared with single-particle cryo-EM reconstruction algorithms, our experimental results suggest this may not be the case. We can recover large changes in latent structure using only 3000 images, a comparatively small dataset by the standards of cryo-EM. Moreover, unlike most common approaches to recovering conformational motions [47], we do not explicitly assume that the viewing direction for each image has been estimated *a priori* but instead draw it

randomly. As our framework is applied to more complex motions and on realistic data, more images may be required, and it may become necessary to integrate more advanced approaches for estimating the viewing direction into our formalism. However, the comparatively small number of images required in our initial results suggests that gradient flows can function with realistic dataset sizes.

A key contribution of this work is the adoption of an optimize-then-discretize (OTD) strategy. An alternate approach would be the discretize-then-optimize (DTO) paradigm, where we first introduce an approximate family of probability densities and then solve an optimization problem. Employing an OTD approach has several theoretical advantages and allows for better flexibility in representing structural heterogeneity by avoiding early discretization of the solution space. In contrast, DTO approaches are often easier to derive. As a theoretical contribution, we observe that the MAP approaches used in software such as RELION and CryoSPARC can be considered examples of DTO approaches. As the nontrivial dependence of these algorithms on the choice of discretization complicates their analysis, we give consistency conditions for generic DTO schemes.

In all, our work illustrates the potential benefits of modeling structural inference problems using the geometry of optimal transport. This formulation supports a natural interpretation of the reconstruction process as a gradient flow over probability distributions. In future work, we aim to conduct a comprehensive convergence analysis for the proposed particle method, as well as explore and benchmark the space of possible gradient-flow cryo-EM algorithms using experimental cryo-EM data. More broadly, the proposed framework is not limited to cryo-EM and may be adapted to other inverse problems that involve learning distributions over latent variables from noisy, high-dimensional observations.

REFERENCES

- [1] F. Abraham, M. Behr, and M. Heinkenschloss. The effect of stabilization in finite element methods for the optimal boundary control of the Oseen equations. *Finite Elements in Analysis and Design*, 41(3):229–251, 2004.
- [2] I. Bahar, T. R. Lezon, L.-W. Yang, and E. Eyal. Global dynamics of proteins: bridging between structure and function. *Annual Review of Biophysics*, 39:23–42, 2010.
- [3] P. R. Baldwin, Y. Z. Tan, E. T. Eng, W. J. Rice, A. J. Noble, C. J. Negro, M. A. Cianfrocco, C. S. Potter, and B. Carragher. Big data in cryoEM: automated collection, processing and accessibility of EM data. *Current Opinion in Microbiology*, 43:1–8, 2018. Environmental Microbiology * The New Microscopy.
- [4] J. Bradbury, R. Frostig, P. Hawkins, M. J. Johnson, C. Leary, D. Maclaurin, G. Necula, A. Paszke, J. VanderPlas, S. Wanderman-Milne, and Q. Zhang. JAX: composable transformations of Python+NumPy programs, 2018.
- [5] A. Braides. A handbook of Γ -convergence. In *Handbook of Differential Equations: stationary partial differential equations*, volume 3, pages 101–213. Elsevier, 2006.
- [6] J. Breidt, T. Butler, and D. Estep. A measure-theoretic computational method for inverse sensitivity problems I: Method and analysis. *SIAM Journal on Numerical Analysis*, 49(5):1836–1859, 2011.
- [7] J. Burkardt, M. Gunzburger, and J. Peterson. Insensitive functionals, inconsistent gradients, spurious minima, and regularized functionals in flow optimization problems. *International Journal of Computational Fluid Dynamics*, 16(3):171–185, 2002.
- [8] T. Butler and D. Estep. A numerical method for solving a stochastic inverse problem for parameters. *Annals of Nuclear Energy*, 52:86–94, 2013.
- [9] T. Butler, D. Estep, and J. Sandelin. A computational measure theoretic approach to inverse sensitivity problems II: A posteriori error analysis. *SIAM Journal on Numerical Analysis*, 50(1):22–45, 2012.
- [10] T. Butler, D. Estep, S. Tavener, C. Dawson, and J. J. Westerink. A measure-theoretic computational method for inverse sensitivity problems III: Multiple quantities of interest. *SIAM/ASA Journal on Uncertainty Quantification*, 2(1):174–202, 2014.
- [11] E. Callaway. The revolution will not be crystallized: a new method sweeps through structural biology. *Nature*, 525(7568):172–174, 2015.
- [12] B. Carragher, Y. Cheng, A. Frost, R. M. Glaeser, G. C. Lander, E. Nogales, and H.-W. Wang. Current outcomes when optimizing ‘standard’ sample preparation for single-particle cryo-EM. *Journal of microscopy*, 276(1):39–45, 2019.
- [13] Y.-C. Chen. A tutorial on kernel density estimation and recent advances, 2017.
- [14] C. Chothia and A. M. Lesk. The relation between the divergence of sequence and structure in proteins. *The EMBO Journal*, 5(4):823–826, 1986.
- [15] CryoJAX Developers. Cryojax documentation. <https://github.com/your-library-link>, 2025. Accessed:

- 2025-03-24.
- [16] K. A. Dill and J. L. MacCallum. The protein-folding problem, 50 years on. *Science*, 338(6110):1042–1046, 2012.
 - [17] R. M. Dudley. *Real analysis and probability*. Chapman and Hall/CRC, 2018.
 - [18] A. Faruqi and R. Henderson. Electronic detectors for electron microscopy. *Current Opinion in Structural Biology*, 17(5):549–555, 2007. Carbohydrates and glycoconjugates / Biophysical methods.
 - [19] J. Frank. *Three-Dimensional Electron Microscopy of Macromolecular Assemblies: Visualization of Biological Molecules in Their Native State*. Oxford University Press, 03 2006.
 - [20] J. Frank and A. Ourmazd. Continuous changes in structure mapped by manifold embedding of single-particle data in cryo-EM. *Methods*, 100:61–67, 2016. Single Particle Cryo-EM, from sample to reconstruction.
 - [21] M. A. Gilles and A. Singer. Cryo-EM heterogeneity analysis using regularized covariance estimation and kernel regression. *Proceedings of the National Academy of Sciences*, 122(9):e2419140122, 2025.
 - [22] R. M. Glaeser. How good can cryo-EM become? *Nature Methods*, 13(1):28–32, 2016.
 - [23] D. S. Goodsell and A. J. Olson. Structural symmetry and protein function. *Annual Review of Biophysics and Biomolecular Structure*, 29:105 – 153, 2000. Cited by: 778.
 - [24] W. W. Hager. Runge-Kutta methods in optimal control and the transformed adjoint system. *Numerische Mathematik*, 87(2):247–282, 2000.
 - [25] T. Haliloglu, I. Bahar, and B. Erman. Gaussian dynamics of folded proteins. *Phys. Rev. Lett.*, 79:3090–3093, Oct 1997.
 - [26] R. Henderson. The potential and limitations of neutrons, electrons and x-rays for atomic resolution microscopy of unstained biological molecules. *Quarterly Reviews of Biophysics*, 28(2):171–193, 1995.
 - [27] J. R. Horn and B. K. Shoichet. Allosteric inhibition through core disruption. *Journal of Molecular Biology*, 336(5):1283–1291, 2004.
 - [28] K. Jamali, L. Käll, R. Zhang, A. Brown, D. Kimanius, and S. H. W. Scheres. Automated model building and protein identification in cryo-EM maps. *Nature*, 628(8007):450–457, 2024.
 - [29] D. Kimanius, L. Dong, G. Sharov, T. Nakane, and S. H. Scheres. New tools for automated cryo-EM single-particle analysis in RELION-4.0. *Biochemical Journal*, 478(24):4169–4185, 2021.
 - [30] W. Kühlbrandt. The resolution revolution. *Science*, 343(6178):1443–1444, 2014.
 - [31] Q. Li, M. Oprea, L. Wang, and Y. Yang. Stochastic Inverse Problem: stability, regularization and Wasserstein gradient flow. *arXiv preprint arXiv:2410.00229*, 2024.
 - [32] Q. Li, M. Oprea, L. Wang, and Y. Yang. Inverse problems over probability measure space. *arXiv preprint arXiv:2504.18999*, 2025.
 - [33] Q. Li, L. Wang, and Y. Yang. Differential Equation–Constrained Optimization with Stochasticity. *SIAM/ASA Journal on Uncertainty Quantification*, 12(2):549–578, 2024.
 - [34] A. Moscovich, A. Halevi, J. Andén, and A. Singer. Cryo-EM reconstruction of continuous heterogeneity by Laplacian spectral volumes. *Inverse Problems*, 36(2):024003, jan 2020.
 - [35] T. Nakane, A. Kotecha, A. Sente, G. McMullan, S. Masiulis, P. M. G. E. Brown, I. T. Grigoras, L. Malinauskaitė, T. Malinauskas, J. Miehl, T. Uchański, L. Yu, D. Karia, E. V. Pechnikova, E. de Jong, J. Keizer, M. Bischoff, J. McCormack, P. Tiemeijer, S. W. Hardwick, D. Y. Chirgadze, G. Murshudov, A. R. Aricescu, and S. H. W. Scheres. Single-particle cryo-EM at atomic resolution. *Nature*, 587(7832):152–156, 2020.
 - [36] A. Punjani and D. J. Fleet. 3D variability analysis: Resolving continuous flexibility and discrete heterogeneity from single particle cryo-EM. *Journal of structural biology*, 213(2):107702, 2021.
 - [37] A. Punjani, J. L. Rubinstein, D. J. Fleet, and M. A. Brubaker. cryoSPARC: algorithms for rapid unsupervised cryo-EM structure determination. *Nature Methods*, 14(3):290–296, 2017.
 - [38] A. Punjani, H. Zhang, and D. J. Fleet. Non-uniform refinement: adaptive regularization improves single-particle cryo-EM reconstruction. *Nature Methods*, 17(12):1214–1221, 2020.
 - [39] S. H. Scheres. A Bayesian view on cryo-EM structure determination. *Journal of Molecular Biology*, 415(2):406–418, 2012.
 - [40] S. H. Scheres. RELION: implementation of a Bayesian approach to cryo-EM structure determination. *Journal of Structural Biology*, 180(3):519–530, 2012.
 - [41] D. Sejdinovic, B. Sriperumbudur, A. Gretton, and K. Fukumizu. Equivalence of distance-based and RKHS-based statistics in hypothesis testing. *The Annals of Statistics*, 41(5), Oct. 2013.
 - [42] A. K. Shiau, S. F. Harris, D. R. Southworth, and D. A. Agard. Structural analysis of E. coli hsp90 reveals dramatic nucleotide-dependent conformational rearrangements. *Cell*, 127(2):329–340, 2006.
 - [43] F. J. Sigworth. Principles of cryo-EM single-particle image processing. *Microscopy*, 65(1):57–67, 12 2015.
 - [44] A. M. Stuart. Inverse problems: a Bayesian perspective. *Acta numerica*, 19:451–559, 2010.
 - [45] S. Subramaniam, W. Kühlbrandt, and R. Henderson. CryoEM at **IUCrJ**: a new era. *IUCrJ*, 3(1):3–7, Jan 2016.
 - [46] W. S. Tang, D. Silva-Sánchez, J. Giraldo-Barreto, B. Carpenter, S. M. Hanson, A. H. Barnett, E. H. Thiede, and P. Cossio. Ensemble Reweighting Using Cryo-EM Particle Images. *The Journal of Physical Chemistry B*, 127(24):5410–5421, 2023.
 - [47] W. S. Tang, E. D. Zhong, S. M. Hanson, E. H. Thiede, and P. Cossio. Conformational heterogeneity and probability distributions from single-particle cryo-electron microscopy. *Current Opinion in Structural Biology*, 81:102626, 2023.

- [48] M. M. Tirion. Large amplitude elastic motions in proteins from a single-parameter, atomic analysis. *Phys. Rev. Lett.*, 77:1905–1908, Aug 1996.
- [49] A. Uzman. Molecular biology of the cell (4th ed.): Alberts, b., johnson, a., lewis, j., raff, m., roberts, k., and walter, p. *Biochemistry and Molecular Biology Education*, 31(4):212–214, 2003.
- [50] A. Vadeboncoeur, M. Girolami, and A. M. Stuart. Efficient Deconvolution in Populational Inverse Problems. *arXiv preprint arXiv:2505.19841*, 2025.
- [51] S. Zhang, J. M. Krieger, Y. Zhang, C. Kaya, B. Kaynak, K. Mikulska-Ruminska, P. Doruker, H. Li, and I. Bahar. ProDy 2.0: increased scale and scope after 10 years of protein dynamics modelling with python. *Bioinformatics*, 37(20):3657–3659, 2021.
- [52] E. D. Zhong, T. Bepler, B. Berger, and J. H. Davis. CryoDRGN: reconstruction of heterogeneous cryo-EM structures using neural networks. *Nature Methods*, 18(2):176–185, 2021.